

Learning Rigidity in Dynamic Scenes with a Moving Camera for 3D Motion Field Estimation

Zhaoyang Lv^{1*}, Kihwan Kim², Alejandro Troccoli², Deqing Sun²,
James M. Rehg¹, Jan Kautz²

¹ Georgia Institute of Technology
{zhaoyang.lv,rehg}@gatech.edu

² NVIDIA
{kihwan,atroccoli,deqings,jkautz}@nvidia.com

Abstract. Estimation of 3D motion in a dynamic scene from a temporal pair of images is a core task in many scene understanding problems. In real world applications, a dynamic scene is commonly captured by a moving camera (i.e., panning, tilting or hand-held), increasing the task complexity because the scene is observed from different view points. The main challenge is the disambiguation of the camera motion from scene motion, which becomes more difficult as the amount of rigidity observed decreases, even with successful estimation of 2D image correspondences. Compared to other state-of-the-art 3D scene flow estimation methods, in this paper we propose to *learn* the rigidity of a scene in a supervised manner from a large collection of dynamic scene data, and directly infer a rigidity mask from two sequential images with depths. With the learned network, we show how we can effectively estimate camera motion and projected scene flow using computed 2D optical flow and the inferred rigidity mask. For training and testing the rigidity network, we also provide a new semi-synthetic dynamic scene dataset (synthetic foreground objects with a real background) and an evaluation split that accounts for the percentage of observed non-rigid pixels. Through our evaluation we show the proposed framework outperforms current state-of-the-art scene flow estimation methods in challenging dynamic scenes.

Keywords: Rigidity Estimation, Dynamic Scene Analysis, Scene Flow Estimation

1 Introduction

The estimation of 3D motion from images is a fundamental computer vision problem, and key to many applications such as robot manipulation [1], dynamic scene reconstruction [2, 3], autonomous driving [4–7], action recognition [8], and video analysis [9]. This task is commonly referred as *3D motion field* or *scene flow estimation*. 3D motion field estimation in a dynamic environment is, however, a challenging and still open problem when the scene is observed from

* This work started during an internship that the author did at NVIDIA.

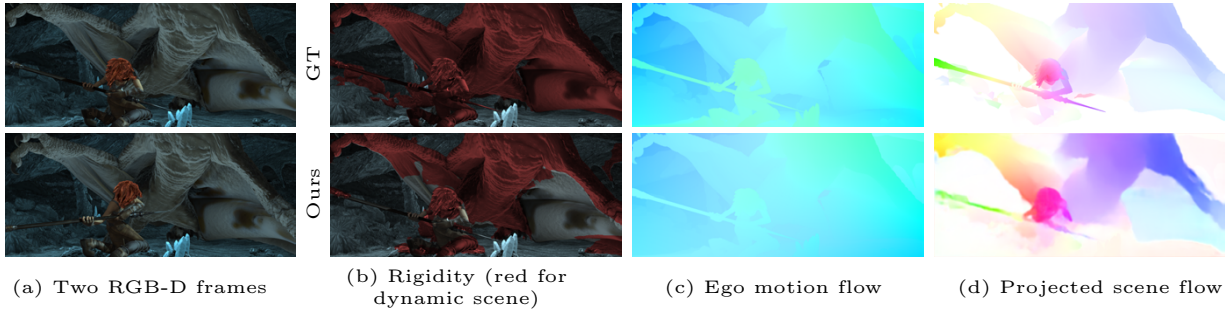


Fig. 1: Our estimated Rigidity (b), Ego-motion Flow (c) and Projected Scene Flow (d) (bottom row) compared to the ground truth (top row). The rigidity mask allows us to solve for the relative camera transform and compute the 3D motion field given the optical flow.

different view points and the amount of coverage of moving objects (either rigid or non-rigid) in each image is large. This is mainly because the disambiguation of camera motion (ego-motion) from object motion requires the correct identification of *rigid static structure* of a scene. Unlike other methods solving the problem with piecewise rigid motion [10, 11], clustering local motions [12], and semantic segmentation [13, 14], we directly *learn* the rigidity of a scene from large scale dynamic scene data, and infer the per-pixel rigidity mask from each image. Fig. 1 shows an example of our estimated rigidity mask, estimated scene flow (projected scene flow for the visualization) compared to ground-truth.

Our framework, shown in Fig. 2, takes a two sequential image pair with color and depth (RGBD) as the input and mainly focuses on dynamic scenes with a moving camera (i.e., panning), where camera motion and objects motions are entangled in each observation. To solve for 2D correspondences, our framework relies on 2D optical flow, and is not tied to any particular algorithm. We use the method by Sun et al. [15], which we evaluate together with the rigidity network to estimate both ego-motion and scene-motions. The network that learns the per-pixel rigidity also solves for the relative camera pose between two images, and this estimated pose is refined in later stages constrained by the 2D optical flow computed from the image pair. To provide better supervision during training and encourage generalization, we develop a tool and methodology that enables the creation of a scalable semi-synthetic RGB-D dynamic scene dataset, which we call *REFRESH*. This dataset combines real-world static rigid background with non-rigid synthetic human motions [16] and provides ground truth color, depth, optical flow and camera pose.

In summary, our major contributions are:

1. A learning-based rigidity and pose estimation algorithm for dynamic scenes with a moving camera.
2. An RGBD 3D motion field estimation framework that builds on inference from rigidity, pose, and existing 2D optical flow, which outperforms the state-of-the-art methods.
3. A new semi-synthetic dynamic scene data and its creation tool: REal 3D From REconstruction with Synthetic Humans (REFRESH). We will make the dataset and software publicly available.

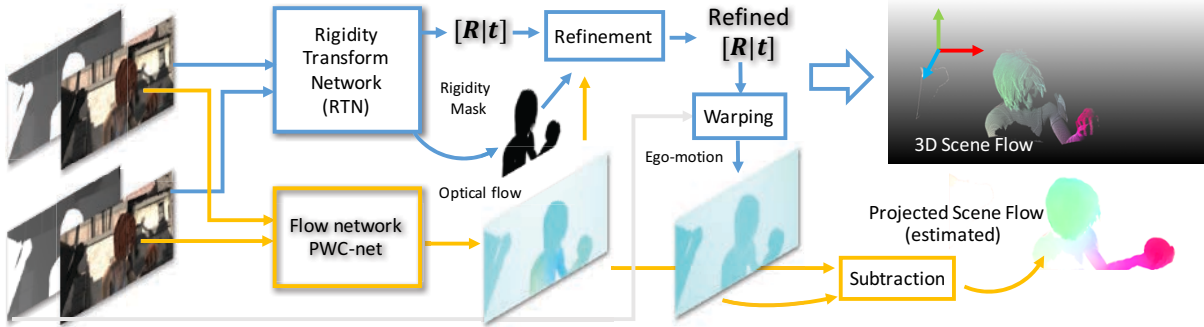


Fig. 2: An overview of our proposed inference architecture for 3D motion field estimation. Our method takes two RGB-D frames as inputs that are processed independently by two networks. The Rigidity Transform Network (RTN) estimates the relative camera transform and rigid/non-rigid regions. Meanwhile, the flow network [15] computes 2D optical flow. We further refine the relative camera transform with the optical flow over the rigid region. With the refined pose, we compute 3D motion field and projected scene flow from the egomotion flow.

2 Related Work

3D scene flow estimation in dynamic scenes brings together fundamental computer vision algorithms such as 2D optical flow, and pose estimation of camera and objects. Furthermore, identifying rigid motions in a dynamic environment plays an important role in tasks requiring epipolar consistency (i.e., motion segmentation [12, 17] or RANSAC algorithms [18, 19]). In the following section, we enumerate pieces of work that inspired our method or are relevant to our work.

Scene Flow: Vedula et al. [20] defined the 3D motion field as *scene flow*, and proposed a method to compute *dense non-rigid* 3D motion fields from a fixed multi-view set-up. The extension to a moving camera case requires us to disambiguate the camera ego-motion from object scene motions in 3D. Due to the intrinsic complexity of such task, existing methods often address it using a variational approach with known camera parameters [21, 22] or assume scene motions are piecewise rigid [11, 18, 19, 23–25]. When depth is known, scene flow can be more accurately estimated. Quiroga et al. model RGB-D scene flow as a rigid flow induced from a composition of camera motion and non-rigid 6DoF transforms [26]. Sun et al. present a joint probabilistic inference approach to solve the camera and scene motions as a composition of finite rigid moving objects [13]. Jaimez et al. segment the scene into static and non-static region, and separately solve camera motion in static region and non-static regions as moving clustered patches, being the first to achieve real-time scene flow estimation [12]. They solve the rigidity segmentation based on the robust residuals of two frame alignment, which is similarly used in [3, 17] for camera tracking in dynamic environments. All of these approaches use rigidity as a prior, but can fail as the complexity of the dynamic scene increases. None of these methods use learned models. We

show that the 3D motion field can be more accurately estimated using learned models for rigidity and optical flow.

In this paper we focus on solving for the 3D motion field in the physical scene observed from a moving camera, commonly named as scene flow [12, 20]. Note that the 3D motion field in a physical scene is not identical to the two-view 3D correspondences in the image space, as discussed in Section 3 and Figure 3.

Learning Camera Transform and Rigidity: Recently, various learning-based methods have been introduced for the joint estimation of camera transform and depth (or rigid structure) [27–29], and scene motion under rigid-body transform [1]. Most of these approaches assume that the scene is either static [27], quasi-static (the amount of scene motions is minimal and they can be dealt as outliers) [29], or that the camera is static when a rigid scene motion occurs [1, 28]. More recently, a few approaches [14, 30] demonstrated the importance of learning *rigidity* to handle dynamic scenes. Wulff et al. [14] assume the rigidity can be derived from the semantic segmentation labels of a single image, while we posit that rigidity is intrinsically related to motion and the two-view geometry. Yin and Shi [30] show that learning the non-rigid flow residual helps their 3D unsupervised scene reconstruction trained on KITTI. In our approach, we are interested in more general dynamic scenes where scene motion region is higher while camera moves, and we address this by directly learning the per-pixel rigidity in the supervised manner which can generalize to new scenes.

Synthetic Dataset for Learning Scene Motion: Synthetic datasets with ground-truth are essential for training modern computer vision algorithms, especially when acquiring ground truth from real world data is difficult or infeasible [31–35]. Optical flow models have been trained using rendered animations like SINTEL and Monka, and frames captured from games [31, 33, 35]. Collections of 3D object models [36, 37] are very useful for rendering new synthetic datasets with known and varying camera pose [38, 33]. Byravan et al. render purely synthetic rigid motion in 3D [1]. Varol et al. create synthetic human motions by bootstrapping human models that follow real motion from motion captured data [39, 16]. Among all of these datasets, only FlyingThings3D [33] provides sufficient 3D training samples for learning 3D flow with moving camera ground truth. However, it uses a small set of 3D objects with textured images at infinity as static scene context and rigid objects as the dynamic scene, which do not provide realistic scene structure for motion estimation. SINTEL [31] has very little variation and a small number of frames, so we use it for testing instead of training. To overcome this data limitation, we have developed a dataset creation method and created a new dataset for RGB-D scene flow training with real-world acquired RGB-D sequences that are augmented with rendered non-rigid moving human models. Compared to FlyingThings3D [33] which only uses rigid moving objects, we use synthetic humans without any other rigid objects since human motions are representative of general non-rigidity and most commonly observed in real world scenes.

3 Rigidity, Scene Flow and Moving Camera

Here we define the relationship between 2D image correspondences and scene flow in physical 3D scenes with object motions and camera motion derived from relative camera poses between two temporal views.

Let $\mathbf{x}_t \in \mathbb{R}^3$ be the location of a point \mathbf{x} on a non-rigid surface Ω_t of a moving object with respect to a fixed world coordinate system at time t . We define $\delta\mathbf{x}_{t \rightarrow t+1}$ as the 3D motion vector of \mathbf{x} from time t to time $t+1$, also referred as scene flow in this paper. When \mathbf{x}_t is observed by a camera with known intrinsics, we define $\pi(\mathbf{x}_t)$ to be the projection of \mathbf{x}_t to image coordinates \mathbf{u}_t , and $\pi^{-1}(\mathbf{u}_t, z_t)$ the inverse projection into 3D camera coordinates given the known depth z_t in the camera reference frame.

Scene flow, 2D Optical Flow, and Camera Pose Optical flow offers direct 2D associations of measurements in I_t and I_{t+1} . Suppose \mathcal{C}_t is the known camera extrinsics matrix for I_t , then the optical flow $\delta\mathbf{u}_{t \rightarrow t+1}$ from I_t to I_{t+1} can be defined as follows:

$$\delta\mathbf{u}_{t \rightarrow t+1}^{of} = \pi(\mathcal{C}_{t+1}(\mathbf{x}_t + \delta\mathbf{x}_{t \rightarrow t+1})) - \pi(\mathcal{C}_t\mathbf{x}_t) \quad (1)$$

Equation 1 states the two-view geometric relationship between 2D optical flow and 3D scene flow. We can simplify it by considering the camera's relative motion

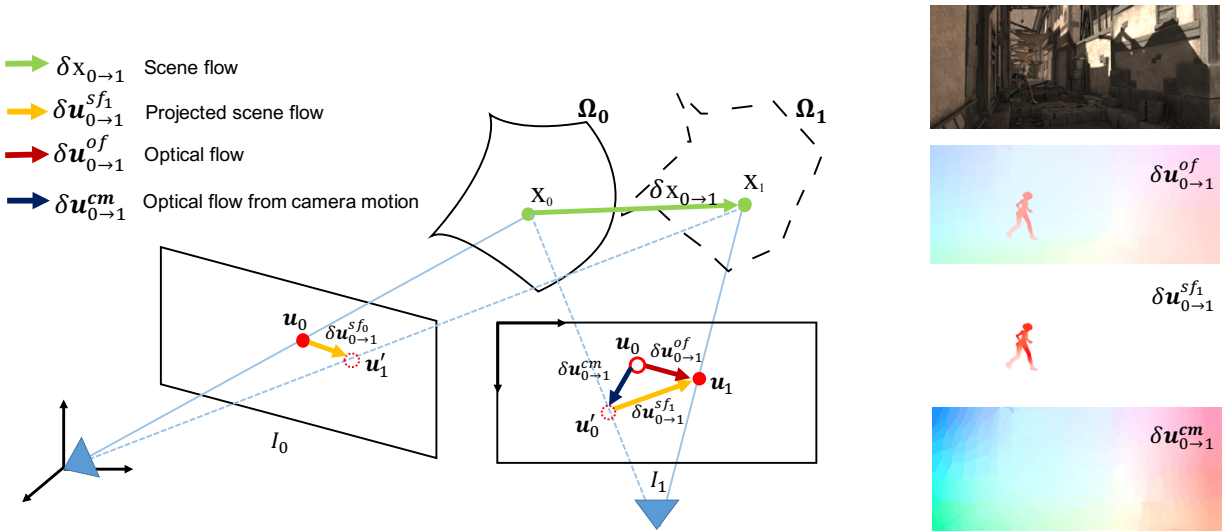


Fig. 3: Two-frame scene flow in a dynamic scene. We show the geometry of a dynamic scene where the camera moves from I_0 to I_1 , and point \mathbf{x}_0 moves to \mathbf{x}_1 (denoted as green circles), and their projections in the two images are shown as $\mathbf{u}_0, \mathbf{u}_1$ respectively (red circles). Note that \mathbf{u}'_0 is a projected location of \mathbf{x}_0 in I_1 , as if \mathbf{x}_0 were observed by I_1 , and can be computed by camera motion as $\delta\mathbf{u}_{0 \rightarrow 1}^{cm}$, and \mathbf{u}_0 in I_1 is visualizing the pixel location it had in I_0 . If the camera was static and observed both \mathbf{x}_0 and \mathbf{x}_1 at the position of I_1 , optical flow $\delta\mathbf{u}_{0 \rightarrow 1}^{of}$ would be same to a projected scene flow $\delta\mathbf{u}_{0 \rightarrow 1}^{sf_1}$. The right image shows each flow in I_1 of dynamic scene under camera panning.

from I_0 to I_1 , i.e. assuming $t = 0$ and setting \mathcal{C}_0 to identity:

$$\delta \mathbf{u}_{0 \rightarrow 1}^{of} = \pi(\mathcal{C}_1(\mathbf{x}_0 + \delta \mathbf{x}_{0 \rightarrow 1})) - \pi(\mathbf{x}_0) \quad (2)$$

Given the optical flow $\delta \mathbf{u}_{0 \rightarrow 1}^{of}$ and the depth from the RGBD data, the 3D scene flow vector can be computed as:

$$\delta \mathbf{x}_{0 \rightarrow 1} = \mathcal{C}_1^{-1} \pi^{-1}(\mathbf{u}_0 + \delta \mathbf{u}_{0 \rightarrow 1}^{of}, z_1) - \pi^{-1}(\mathbf{u}_0, z_0) \quad (3)$$

Note that \mathcal{C}_1 can be computed from 2D correspondences that follow two-view epipolar geometry [40], and the corresponding points should lie on the rigid and static background structure. This is especially challenging when the scene contains dynamic components (moving objects) as well as a rigid and stationary background structure. As such, identifying inliers and outliers using *rigidity* is a key element for successful relative camera pose estimation, and thus is necessary to achieve reaching accurate scene flow estimation in a dynamic scene [41, 12], which we will discuss in Sec. 4.

Egomotion Flow from a Moving Camera in a Static Scene: When an observed \mathbf{x} in a scene remains static between the two frames, $\delta \mathbf{x}_{0 \rightarrow 1} = \mathbf{0}$ and therefore $\mathbf{x}_1 = \mathbf{x}_0$. Then, the observed optical flow is purely induced by the camera motion and we refer it as a camera egomotion flow:

$$\delta \mathbf{u}_{0 \rightarrow 1}^{cm} = \pi(\mathcal{C}_1 \mathbf{x}_0) - \pi(\mathbf{x}_0) \quad (4)$$

Projected Scene Flow and Rigidity: As described in Figure 3, the projected scene flow is a projection of a 3D scene flow $\delta \mathbf{x}_{0 \rightarrow 1}$ in I_1 if \mathbf{x}_0 was observed from I_1 , which can be computed from camera ego-motion and optical flow:

$$\delta \mathbf{u}_{0 \rightarrow 1}^{sf} = \delta \mathbf{u}_{0 \rightarrow 1}^{of} - \delta \mathbf{u}_{0 \rightarrow 1}^{cm} \quad (5)$$

The projected scene flow (in a novel view) is also referred as non-rigid residual [26, 30]. All locations with zero values in projected scene flow indicate the rigidity region in ground truth data. As demonstrated in Figure 3, the projected scene flow is a useful tool to evaluate the results of dense scene flow estimation in the 2D domain which requires accurate estimation of both camera pose and optical flow. Thus, we use it as the evaluation metric in Sec. 6.

4 3D Motion Field Estimation Pipeline

With the relationship between scene flow, optical flow and relative camera pose now established, we introduce a framework that refines the relative camera transform and the optical flow with a rigidity mask for accurate scene flow estimation. Figure 2 shows the overview of our proposed pipeline. Given a temporal pair of RGB-D images, we concurrently run the optical flow and rigidity-transform network. The optical flow network [15] offers the 2D correspondence association between frames, and our proposed rigidity-transform network provides an estimate of the camera transform and the rigidity mask.

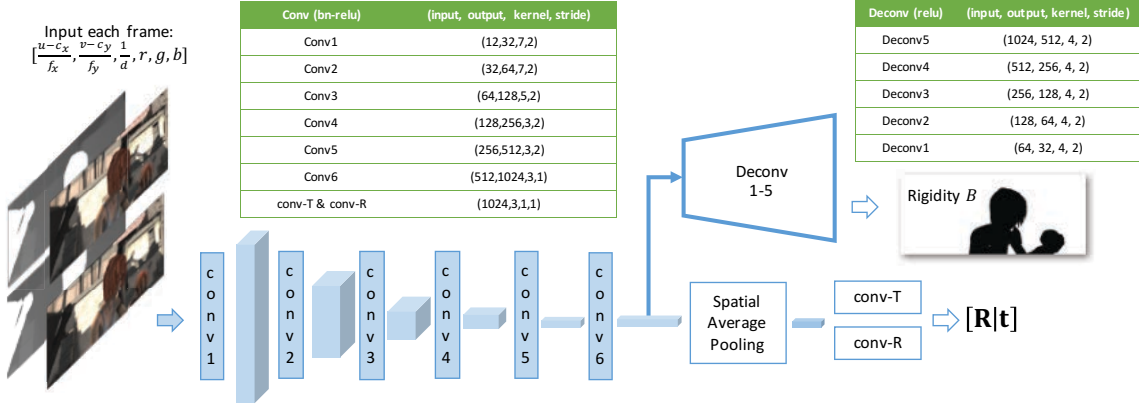


Fig. 4: **Rigidity-Transform network (RTN) architecture** The inputs to the RTN are 12 channel tensors encoded with $[(u - c_x)/f_x, (v - c_y)/f_y, 1/d, r, g, b]$ computed from a pair of RGB-D images and their intrinsics. It is a fully convolutional encoder-decoder architecture predicting pose as a translation and euler angles, and scene rigidity as a binary mask.

4.1 Rigidity-Transform Network

Previous work on camera pose estimation using CNNs focused on either purely static or quasi-static scenes, where scene motions are absent or their amount is minimal [27–29]. In dynamic scenes with a moving camera, camera pose estimation can be challenging due to the ambiguity induced by the camera motion and scene (object) motion. Existing solutions disambiguate the two using prior information in motion or semantic knowledge [12, 13, 26, 42]. We propose to replace this hand-coded criteria by a fully-convolutional network that jointly learns camera motion and a segmentation of the scene into dynamic and static regions. We represent this rigidity segmentation as a binary mask with the static scene masked as rigid. The rigid scene components will obey the epipolar constraints induced by the camera ego-motion and serve as the regions of *attention of the camera transform*. We name it rigidity-transform network (RTN), shown in Fig. 4.

RTN: Given a pair of RGB-D frames, we pre-process each frame into a 6 channel tensor $[(u - c_x)/f_x, (v - c_y)/f_y, 1/d, r, g, b]$, from camera intrinsics parameters $[f_x, f_y, c_x, c_y]$ and the depth d . Considering the different range of depth values, this representation is numerical stable in training and delivers good generalization performance. We truncate $1/d$ to the range $[1e-4, 10]$, which is able to cover scenes of various scales. We concatenate the two-frame tensors to a 12-channel tensor as input to our network. The network is composed of an encoder followed by pose regression and a decoder followed by the rigidity segmentation.

Encoder: The encoder is composed of five stride-2 convolutional layers (1-5) which gradually reduce spatial resolution and one stride-1 convolution as the conv-6 layer. Each convolution is followed by a batchnorm and ReLU layer. The target is to predict the camera relative translation \mathbf{t} and rotation Θ . After the conv-6 layer, we use a spatial-average pooling (SAP) to reduce the feature into a $1024D$ vector. With two 1×1 convolution layers that outputs 3

channels, we separately estimate the \mathbf{t} and Θ . We assume the relative camera transformation between two frames is small and thus we represent the rotation $\mathbf{R}(\alpha, \beta, \gamma) = \mathbf{R}_x(\alpha)\mathbf{R}_y(\beta)\mathbf{R}_z(\gamma)$ with Euler angles $\Theta = [\alpha, \beta, \gamma]$. The regression loss is a weighted combination of the robust Huber loss $\rho(\cdot)$ for translation and rotation as:

$$\mathcal{L}_p = \rho(\mathbf{t} - \mathbf{t}^*) + w_\Theta \rho(\Theta - \Theta^*) \quad (6)$$

Decoder: The decoder network is composed of five deconvolution (transpose convolution) layers which gradually upsample the conv-6 feature into input image scale and reshape it into the original image resolution. We estimate the rigidity attention as a binary segmentation problem with binary cross-entropy loss \mathcal{L}_r . The overall loss is a weighted sum of both loss functions: $\mathcal{L}_c = w_p \mathcal{L}_p + \mathcal{L}_r$.

Enforcing Network Learning from Two Views: To learn the rigid regions of two views, we enforce the network to capture both scene structures and epipolar constraints w.r.t. two views from two aspects. First, our network is fully convolutional and we regress the camera pose from the SAP layer which preserves feature distributions spatially. Features for rigidity segmentation and pose regression can interact directly with each other spatially across each feature map. We do not use any skip layer connections. Our experiments in Section 6 show simultaneously learning of camera pose and rigidity can help RTN achieve better generalization in complex scenes. Second, we randomly use two identical views as input and a fully rigid mask as output with 20% probability during data augmentation, which prevents the network from only using a single view for its prediction.

4.2 Pose Refinement from Rigidity and Flow

From Section 3 we can compute the 3D motion field given the optical flow and the camera pose. To solve for the 3D motion field accurately from two views, we require a precise camera transformation. The pose output from RTN may not always precisely generalize to new test scenes. To overcome this, we propose a refinement step based on the estimated rigidity B and bidirectional dense optical flow $\delta \mathbf{u}_{0 \rightarrow 1}^{of}$ and $\delta \mathbf{u}_{1 \rightarrow 0}^{of}$ (with forward and backward pass). We view the estimation of \mathcal{C}_1 as a robust least square problem as:

$$\underset{\mathcal{C}_1}{\operatorname{argmin}} \sum_{\{\mathbf{x}_0, \mathbf{x}_1\} \in \Omega(B)} [\mathbf{I}] \rho(\mathcal{C}_1 \mathbf{x}_0 - \mathbf{x}_1) \quad (7)$$

where $\mathbf{x}_i = \pi^{-1}(\mathbf{u}_i, z_i)$ in all background regions B , predicted by the RTN. $[\mathbf{I}]$ is an Iverson bracket for all the inlier correspondences. The inlier correspondences are filtered in several steps. We first use forward backward consistency check for bidirectional optical flow with a threshold of 0.75 to remove all flow correspondences which are not consistent. This generates the occlusion map O . To prevent outliers at the boundary of rigidity B and occlusion O , we use a morphological operator with patch size 10 to dilate B and O . From all correspondences,

we uniformly sample bidirectional flow correspondences with a stride of 4 and select $1e4$ points among them that are closest to the camera viewport. These help to solve the optimization more efficiently and numerically stable. We also use the Huber norm $\rho(\cdot)$ as a robust way to handle the remaining outliers. We solve equation 7 efficiently via Gauss-Newton with \mathcal{C}_1 initialized from the RTN output. With accurate filtered correspondences, the initialization step trivially helps but can also be replaced by an identity initialization.

5 REFRESH Dataset

Supervised training of our networks requires a large scale dataset with a sufficient amount of sequences of RGB-D images over scenes that show dynamic objects and rigid static regions, plus the corresponding ground truth in the form of known camera pose, rigidity mask, and optical flow. To overcome the lack of a suitable dataset, we have created a scene flow dataset: REal 3D from REconstruction with Synthetic Humans, which we name as **REFRESH**. For this task we leverage the success of state of the art 3D reconstruction systems [43–45], which directly provide dense 3D meshes and optimized camera trajectories. We use a pre-captured RGB-D dataset and create dynamic 4D scenes by rendering non-rigid 3D moving objects with pre-defined trajectories. We overlay synthetic objects over the original footage to obtain a composite image with ground truth as shown in Figure 5.

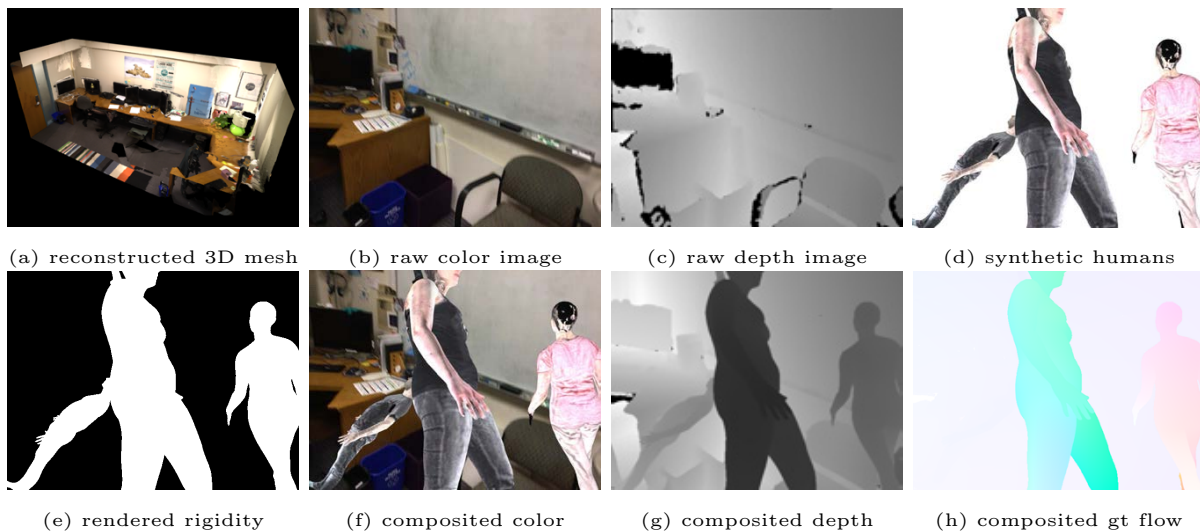


Fig. 5: **REFRESH dataset creation pipeline** With a captured RGB-D trajectory, the scene is reconstructed as a 3D mesh by BundleFusion [43] (a), with raw RGB-D input as (b) and (c). With sampled frames from the camera trajectory, we load synthetic human models [16] with motions randomly into the 3D as (d), and render the rigidity mask (e), Finally we composite the rendered synthetic ground truth with its corresponding rendered 3D views and the final semi-synthetic RGB-D views (f) and (h), with optical flow ground truth as (i).

Real 3D Reconstructed Scenes: We use the 3D meshes created with BundleFusion [43]. The authors released eight reference 3D meshes with the 25K input RGB-D images, camera intrinsics, and solved camera trajectories.

Synthetic humans: We create non-rigid scene elements with the method introduced in SURREAL [16]. Each synthetic body is created from realistic articulated human body models [39]. The articulated human pose actions are from the CMU MoCap database [46] which has more than 20K sequences of 23 action categories. The textures for the human models are composed of SMPL CAESAR scans and real clothing registered with 4Cap [47]. The selection of frames where the created human models will appear, and the properties of the models are randomly chosen. We create each synthetic human with random gender, body shape, cloth texture, and action, which guarantees the diversity of dynamic scenes. We control the visibility of human models along the trajectory by putting the pelvis point of each human model in the free space w.r.t. the ego-centric viewport from a selected frame along the trajectory. The free space is sampled by the corresponding depth. For every 100 frames, we select n frames (n sample from $\sim \mathcal{N}(15, 5)$) and insert n human models into the scene.

Rendering and ground-truth generation: We use Cycles from the Blender ¹ suite as our rendering engine. The lighting is created using spherical harmonics, as in Varol et al. [16]. For every frame we employ a multi-pass rendering approach. First, we set the virtual camera from the known intrinsics of the original scene and match the output resolution. The camera position follows the original trajectory (computed from BundleFusion [43]). We then separately render the 3D reconstructed static mesh and the synthetic humans with the same camera settings, and bring them together using alpha-matting composition. We create the depth map using the rendered depth from the 3D mesh, which is less noisy and more complete than raw depth. Since the camera movement during the 3D acquisition is small between frames, we sub-sample frames at intervals of [1,2,5,10,20] to create larger motions. During rendering we also generate the optical flow image, the rigidity mask, and the camera parameters that make up our ground truth. A visualization of our dataset generation is shown in Figure 5.

6 Experiments

We evaluate our approach under various settings to show the performance of rigidity and pose estimation and their influence on scene flow estimation. For the effective analysis in scenes with different levels of non-rigid motions, we create a new test split from SINTEL data [31] based on the non-rigid number of pixels percentage. We first describe the experimental settings in Section 6.1. In Section 6.2, we discuss our choice of testing examples from SINTEL, and provide a comparison of the performance with different settings for RTN, refinement and other state-of-the-arts methods. In Section 6.3, we provide a qualitative evaluation of our method in real world examples.

¹ Blender: <https://www.blender.org/>



Fig. 6: **Qualitative visualization** on our SINTEL test split. We compare our rigidity prediction with the output using semantic rigidity [14] trained on our REFRESH dataset and our projected scene flow with output of VOSF [12].

6.1 Implementation and Experimental Setting

We implemented the RTN in PyTorch, and the pose refinement in C++ with GTSAM 4.0 [48]. For optical flow correspondence, we use PWCNet [15] implemented in Caffe. We integrate all the modules through Python. We use 68K images from our REFRESH dataset for training². We train RTN from scratch using weight initialization from He et al. [49] and Adam optimizer ($\beta_1 = 0.9$ and $\beta_2 = 0.999$, learning rate of $2e^{-4}$) on 3 GPUs for 16 epochs. During training, the rigidity mask loss is accumulated over 5 different scales. We chose $w_\theta = 1e^2$, which balances the scale of the two losses \mathcal{L}_p and \mathcal{L}_r . We train PWC-net from scratch, with the same training settings and architecture as in Sun et al. [15], a mini-batch size of 12, and we train for 1.2M iterations. We will make the dataset and network publicly available.

² More details about the dataset are included in the appendix section.

Table 1: Quantitative evaluation in flow residuals using SINTEL dataset on our test split. The ratio of Nonrigid (NR) Region indicates the average ratio of pixels in the scene which represents the complexity of dynamic motion in the scene. We report the EPE in egomotion flow (EF) and projected scene flow (PSF). For all the baseline methods in both non-finetuning (NO FT) and finetuning (FT) setting, we use the same optical flow network trained as our method. The lowest residual under the same setting (e.g. NO FT, clean set) is highlighted as **bold**.

		NR Region<10%		NR Region 10%-40%				NR Region>40%		All Test			
		alley_2	temple_2	market_5	ambush_6	cave4		Average					
		EF	PSF	EF	PSF	EF	PSF	EF	PSF	EF	PSF		
CLEAN (no motion blur)													
	(a) SRSF [26]	4.24	7.25	7.59	16.55	25.26	31.67	17.84	37.21	10.77	11.82	12.47	18.57
	(b) VOSF [12]	6.53	1.13	5.13	10.36	16.02	35.24	13.39	28.31	6.05	9.30	8.86	15.24
	(c) Refine only	0.29	0.48	0.90	2.95	8.81	22.34	3.59	14.39	2.18	5.88	3.09	8.47
NO	(d) Semantic[14]+Refine	0.25	0.53	1.07	3.87	5.77	15.74	1.70	9.58	0.85	4.34	1.96	6.42
FT	(e) RTN(no-pose)+Refine	0.13	0.45	0.49	2.79	5.78	16.24	3.72	16.92	1.67	5.37	2.07	7.09
	(f) RTN+Refine	0.18	0.48	0.46	2.72	1.61	11.86	0.97	8.61	0.63	4.05	0.74	5.10
FT	(g) Semantic[14]+Refine	0.19	0.46	0.50	2.73	2.73	13.45	1.13	9.94	2.07	5.87	1.35	5.98
	(h) RTN+Refine	0.18	0.47	0.42	2.64	1.69	11.53	0.47	7.74	0.91	4.34	0.77	5.03
FINAL (with motion blur)													
	(i) SRSF [26]	4.33	7.78	7.59	15.51	24.93	31.29	17.26	39.08	10.80	13.29	12.37	18.86
	(j) VOSF [12]	6.29	1.54	5.69	8.91	15.99	35.17	13.37	24.02	6.23	9.28	8.96	14.61
	(k) Refine only	0.28	0.57	0.90	3.77	8.80	20.64	3.59	20.41	2.18	6.52	3.09	8.95
NO	(l) Semantic[14]+refine	0.25	0.52	0.96	3.83	>100	>100	20.23	35.46	11.05	12.81	>100	>100
FT	(m) RTN(no-pose)+Refine	0.19	0.48	0.82	3.58	2.15	13.97	3.34	20.02	1.52	5.72	1.36	7.14
	(n) RTN+Refine	0.18	0.47	0.88	3.93	0.79	11.87	2.82	19.42	0.66	4.66	0.82	6.29
FT	(o) Semantic[14]+Refine	0.19	0.48	1.91	5.19	1.58	13.02	2.58	19.11	2.13	6.50	1.55	7.39
	(p) RTN+Refine	0.21	0.48	0.66	3.27	0.97	11.35	2.34	19.08	0.74	4.75	0.79	6.12

6.2 Quantitative Evaluation in SINTEL

We evaluate our proposed method on the challenging SINTEL dataset [31], which is a 3D rendered animation containing a sequence of 23 dynamic scenes with cinematic camera motion. The dataset has two versions with different rendering settings: *clean* and *final*. The latter set contains motion blur and depth of field effects, which are not present in the *clean* set. Since the official SINTEL test dataset does not provide RGB-D 3D flow evaluation, we split the SINTEL training set into train, validation, and test split. For the test split, to effectively evaluate and analyze the impact of different levels of non-rigid motions in the estimation, we choose *alley_2* (1.8%), *temp_2* (5.8%), *market_5* (27.04%), *ambush_6* (38.96%), *cave_4* (47.10%), where (\cdot) indicates the average non-rigid regions in each scene sequence. These examples also contain a sufficient amount of camera motion. We use the first 5 frames in the rest of the 18 scenes as a validation set, and the remaining images for training in our finetuning setting.

Table 1 shows our quantitative evaluation. We list the end-point-error (EPE) of the ego-motion flow (EF) and projected scene flow (PSF) as defined in Sec. 3. Our proposed metric overcomes the traditional difficulty of 3D motion flow

Table 2: Quantitative evaluation in relative camera transform using on our SINTEL test split. We report the relative pose error [50] (RPE) composed of translation (t) error and rotation error (r) in Euler angles (degree) in SINTEL depth metric averaged on from outputs using *clean* and *final* pass.

	NR Region <10%		NR Region 10% - 40%				NR Region >40%		All Test			
	alley_2	temple_2	market_5	ambush_6	cave4	AVERAGE						
	RPE(t)	RPE(r)	RPE(t)	RPE(r)	RPE(t)	RPE(r)	RPE(t)	RPE(r)	RPE(t)	RPE(r)		
Orb-SLAM [51]	0.0300	0.0190	0.1740	0.0220	0.1500	0.0160	0.0550	0.0280	0.0167	0.0277	0.0894	0.0218
SRSF [26]	0.0487	0.0141	0.1763	0.0117	0.1566	0.0105	0.0672	0.0729	0.0218	0.0150	0.0980	0.0180
VOSF[12]	0.1043	0.0316	0.1055	0.0155	0.0605	0.0006	0.0375	0.0190	0.0438	0.0046	0.0750	0.0136
Ours (no ft)	0.0015	0.0036	0.0215	0.0010	0.0059	0.0009	0.0153	0.0061	0.0053	0.0009	0.0091	0.0020

evaluation. We compare our method to two state-of-art RGB-D scene flow solutions: SRSF [26] and VO-SF [12]. Both of these methods are optimization-based approaches that explicitly estimate the camera transform as part of the solution to flow correspondence. In addition, we evaluate two other baselines. First one is *refinement only*, which we denote as solving the refinement stage without any information acquired from RTN. This strategy is often used to solve rigid motions by assuming non-rigid motions can be filtered in optimization as high-frequency outliers [3, 12]. Secondly, to demonstrate the performance of our rigidity estimation (RTN), we compare our method to semantic rigidity estimation [14], which assumes that the non-rigid motion can be predicted from its semantic labelling. To fairly evaluate the generalization ability of semantic rigidity w.r.t our RTN, we follow Wulff et al [14] and use the DeepLab [52] architecture with weights initialized from the pre-trained MS-COCO model, but trained over the same data we used for our model. In the pose refinement stage, we substitute our rigidity from RTN with the semantic rigidity. For the fine-tuned evaluation on SINTEL, we re-train both our RTN and the semantic rigidity network. Both baselines use the same optical flow network with the same weights, and all methods use the same depth from SINTEL ground truth. We use the EPE in egomotion flow and projected scene flow defined in Section 3 as a metric. The qualitative comparison is shown in Figure 6.

The results in Table 1 show that: (1) compared to SRSF[26] and VOSF [12], our proposed algorithm with learned rigidity can improve scene flow accuracy by a significant margin (rows (a),(b) vs (f); (i),(j) vs (n)); (2) the rigidity mask from our RTN performs better than the single-view semantic segmentation based approach [14], particularly in the more realistic *final pass* setting with no fine-tuning (NO FT)(row (d) vs (e),(f); (l) vs (m),(n)); and (3) as shown in *RTN+refine* setting, the simultaneous learning of rigidity with pose transform also achieves better performance than RTN without pose-regression ((e) vs (f); (m) vs (n)). Furthermore, compared to the semantic rigidity mask [14], which relies on fine-tuning on SINTEL to achieve better performance, our learned rigidity can generalize to unseen complex scenes and perform as well as the fine-tuned model. Our rigidity prediction can capture unseen objects well, as shown by the dragon in Figure 6.

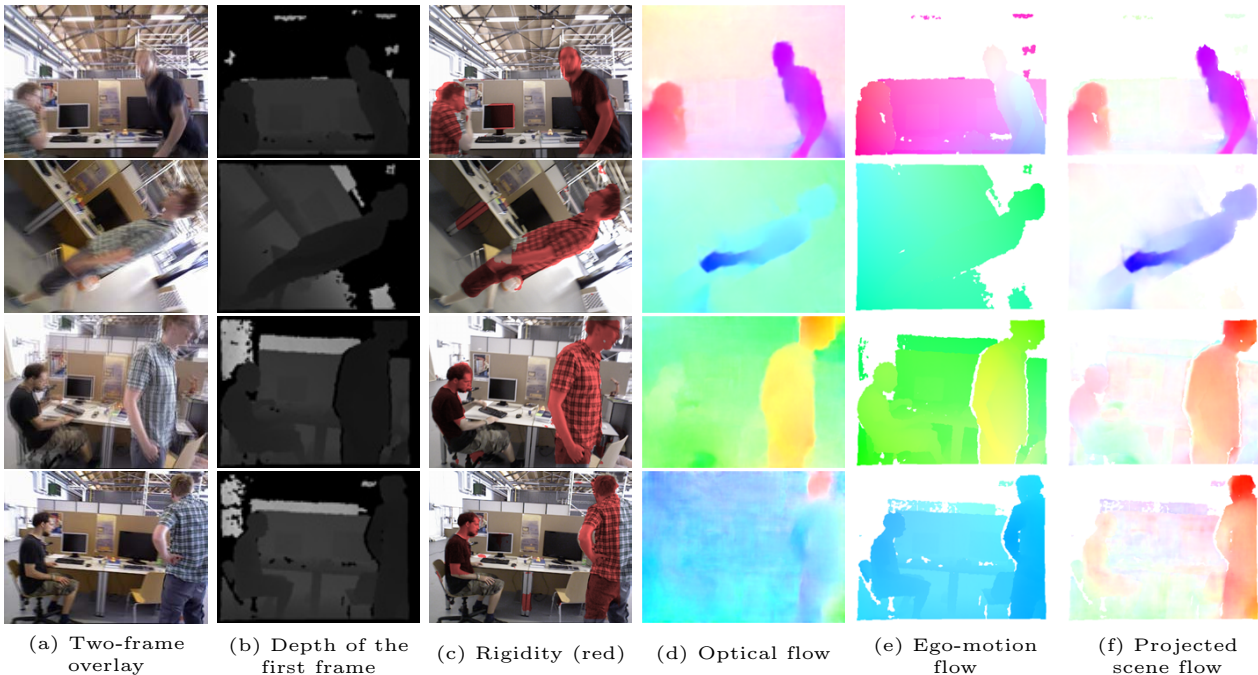


Fig. 7: **Qualitative visualization** of dynamic sequences in TUM [50] sequences.

In Table 2, we evaluate the performance of two-view transform estimation of our method against depth-based ORB-SLAM, SRSF [26] and VOSF[12]. As mentioned, the accuracy of pose estimation in dynamic scenes with moving camera highly relies on the ability ignore the non-rigid surfaces. As shown in the table, our method *without fine-tuning* out-performs the other state-of-the-art methods by a significant margin.

6.3 Evaluation on Real-world Images

To test our algorithm in real-world dynamic scenarios, we use three sequences from the TUM RGB-D datasets [50] which contains dynamic motions observed from a moving Kinect camera. The depth input is noisy with missing observations and the color images contain severe motion blur. We use the raw color and depth input with provided calibrated camera intrinsics as input, and mark the regions as invalid region when the depth value is not within $[0.1, 8]$. In invalid regions, we ignore the rigidity prediction and treat the flow correspondence as outliers. Considering there is no 3D motion flow ground truth for our real data, we visualize the rigidity prediction and projected scene flow to qualitatively show our algorithm performance in Figure 7. Our results show that our trained model on semi-synthetic data can also generalize well to real noisy RGB-D data with significant motion blur. Please refer to the appendix section for a visualization of the sequences.

7 Conclusion and Future Work

We have presented a learning-based approach to estimate the rigid regions in dynamic scenes observed by a moving camera. Furthermore, we have shown that

our framework can accurately compute the 3D motion field (scene flow), and the relative camera transform between two views. To provide better supervision to the rigidity learning task and encourage the generalization of our model, we created a novel semi-synthetic dynamic scene data set, REFRESH, which contains real-world background scenes together with synthetic foreground moving objects. Through various tests we have shown that our proposed method can outperform most state-of-the-art solutions. We also included a new guideline for dynamic scene evaluation with respect to the amount scene motion and camera motion.

We observed some cases where the rigidity mask deviates from the ground-truth. We noticed that in these situations the moving object size is small, or the temporal motions between the two frames are small. However, both the pose computed by our method and the ego-motion flow show small deviations from the ground-truth. As a result, the 3D motion field computed is not affected. The success of the current method also depends on the accuracy of optical flow. In scenarios when optical flow fails or produces noisy correspondences, the errors in correspondences will also propagate to 3D motion field. In future work, we will address both problems by exploiting rendering more diverse datasets to encourage generalization in different scenes. We will also incorporate both rigidity and optical flow to refine the correspondence estimation and explore performance improvements with end-to-end learning, including correspondence refinement and depth estimation from RGB inputs.

Acknowledgment Part of the work in this project was supported by the National Science Foundation and National Robotics Initiative (Grant # IIS-1426998).

References

1. Byravan, A., Fox, D.: SE3-Nets: Learning rigid body motion using deep neural networks. In: IEEE Intl. Conf. on Robotics and Automation (ICRA), IEEE (2017) 173–180
2. Innmann, M., Zollhöfer, M., Nießner, M., Theobalt, C., Stamminger, M.: VolumeDeform: Real-time volumetric non-rigid reconstruction. In: European Conf. on Computer Vision (ECCV). (2016)
3. Newcombe, R.A., Fox, D., Seitz, S.M.: DynamicFusion: Reconstruction and tracking of non-rigid scenes in real-time. In: IEEE Conf. on Computer Vision and Pattern Recognition (CVPR). (June 2015)
4. Geiger, A., Lauer, M., Wojek, C., Stiller, C., Urtasun, R.: 3D traffic scene understanding from movable platforms. IEEE Trans. Pattern Anal. Machine Intell. (2014)
5. Scharwächter, T.,ENZWEILER, M., Franke, U., Roth, S.: Stixmantics: A medium-level model for real-time semantic scene understanding. In: European Conf. on Computer Vision (ECCV). (2014)
6. Shashua, A., Gdalyahu, Y., Hayun, G.: Pedestrian detection for driving assistance systems: Single-frame classification and system level performance. In: IEEE Intelligent Vehicles Symposium (IV). (June 2004) 1–6

7. Wedel, A., Brox, T., Vaudrey, T., Rabe, C., Franke, U., Cremers, D.: Stereoscopic scene flow computation for 3D motion understanding. *Intl. J. of Computer Vision* **95**(1) (2011) 29–51
8. Wang, P., Li, W., Gao, Z., Zhang, Y., Tang, C., Ogunbona, P.: Scene Flow to Action Map: A new representation for RGB-D based action recognition with convolutional neural networks. In: *IEEE Conf. on Computer Vision and Pattern Recognition (CVPR)*. (July 2017)
9. Hung, C.H., Xu, L., Jia, J.Y.: Consistent binocular depth and scene flow with chained temporal profiles. *Intl. J. of Computer Vision* **102**(1-3) (2013) 271–292
10. Vogel, C., Schindler, K., Roth, S.: 3d scene flow estimation with a piecewise rigid scene model. *Intl. J. of Computer Vision* **115**(1) (2015) 1–28
11. Golyanik, V., Kim, K., Maier, R., Nießner, M., Stricker, D., Kautz, J.: Multiframe scene flow with piecewise rigid motion. In: *International Conference on 3D Vision (3DV)*, Qingdao, China (October 2017)
12. Jaimez, M., Kerl, C., Gonzalez-Jimenez, J., Cremers, D.: Fast odometry and scene flow from rgb-d cameras based on geometric clustering. In: *IEEE Intl. Conf. on Robotics and Automation (ICRA)*. (2017)
13. Sun, D., Sudderth, E.B., Pfister, H.: Layered rgb-d scene flow estimation. In: *IEEE Conf. on Computer Vision and Pattern Recognition (CVPR)*, IEEE (2015) 548–556
14. Wulff, J., Sevilla-Lara, L., Black, M.J.: Optical flow in mostly rigid scenes. In: *IEEE Conf. on Computer Vision and Pattern Recognition (CVPR)*. (July 2017)
15. Sun, D., Yang, X., Liu, M.Y., Kautz, J.: PWC-Net: CNNs for optical flow using pyramid, warping, and cost volume. In: *arXiv*. (2017)
16. Varol, G., Romero, J., Martin, X., Mahmood, N., Black, M.J., Laptev, I., Schmid, C.: Learning from Synthetic Humans. In: *CVPR*. (2017)
17. Lv, Z.: *Kinfuseg: a dynamic slam approach based on kinect fusion*. Master’s thesis, Imperial College London (2013)
18. Lv, Z., Beall, C., Alcantarilla, P.F., Li, F., Kira, Z., Dellaert, F.: A continuous optimization approach for efficient and accurate scene flow. In: *European Conf. on Computer Vision (ECCV)*, Springer (2016) 757–773
19. Menze, M., Geiger, A.: Object scene flow for autonomous vehicles. In: *IEEE Conf. on Computer Vision and Pattern Recognition (CVPR)*. (2015) 3061–3070
20. Vedula, S., Baker, S., Rander, P., Collins, R., Kanade, T.: Three-dimensional scene flow. In: *Intl. Conf. on Computer Vision (ICCV)*. Volume 2. (1999) 722–729 vol.2
21. Basha, T., Moses, Y., Kiryati, N.: Multi-view scene flow estimation: A view centered variational approach. In: *IEEE Conf. on Computer Vision and Pattern Recognition (CVPR)*. (2010) 1506–1513
22. Valgaerts, L., Bruhn, A., Zimmer, H., Weickert, J., Stoll, C., Theobalt, C.: Joint estimation of motion, structure and geometry from stereo sequences. In: *European Conf. on Computer Vision (ECCV)*. Volume 6314 LNCS. (2010) 568–581
23. Vogel, C., Schindler, K., Roth, S.: 3D scene flow estimation with a rigid motion prior. In: *Intl. Conf. on Computer Vision (ICCV)*. (2011) 1291–1298
24. Vogel, C., Schindler, K., Roth, S.: Piecewise rigid scene flow. In: *Intl. Conf. on Computer Vision (ICCV)*. (2013) 1377–1384
25. Vogel, C., Schindler, K., Roth, S.: View-consistent 3d scene flow estimation over multiple frames. In: *European Conf. on Computer Vision (ECCV)*. Volume 8692. (2014) 263–278
26. Quiroga, J., Brox, T., Devernay, F., Crowley, J.: Dense semi-rigid scene flow estimation from RGB-D images. In: *European Conf. on Computer Vision (ECCV)*. Volume 8695 LNCS. (2014) 567–582

27. Ummenhofer, B., Zhou, H., Uhrig, J., Mayer, N., Ilg, E., Dosovitskiy, A., Brox, T.: DeMoN: depth and motion network for learning monocular stereo. In: IEEE Conf. on Computer Vision and Pattern Recognition (CVPR). (2017)
28. Vijayanarasimhan, S., Ricco, S., Schmid, C., Sukthankar, R., Fragkiadaki, K.: SfM-Net: learning of structure and motion from video. arXiv [abs/1704.07804](https://arxiv.org/abs/1704.07804) (2017)
29. Zhou, T., Brown, M., Snavely, N., Lowe, D.G.: Unsupervised learning of depth and ego-motion from video. In: CVPR. (2017)
30. Yin, Z., Shi, J.: GeoNet: Unsupervised Learning of Dense Depth, Optical Flow and Camera Pose. Technical Report arXiv:1803.02276 [cs.CV] (2018)
31. Butler, D.J., Wulff, J., Stanley, G.B., Black, M.J.: A naturalistic open source movie for optical flow evaluation. In: European Conf. on Computer Vision (ECCV), The Royal Society (2012) 611–625
32. Gu, J., Yang, X., Mello, S.D., Kautz, J.: Dynamic facial analysis: From bayesian filtering to recurrent neural networks. In: CVPR. (2016)
33. Mayer, N., Ilg, E., Hausser, P., Fischer, P., Cremers, D., Dosovitskiy, A., Brox, T.: A large dataset to train convolutional networks for disparity, optical flow, and scene flow estimation. In: IEEE Conf. on Computer Vision and Pattern Recognition (CVPR). (2016) 4040–4048
34. Kim, K., Gu, J., Tyree, S., Molchanov, P., Nießner, M., Kautz, J.: A lightweight approach for on-the-fly reflectance estimation. In: ICCV. (2017)
35. Richter, S.R., Hayder, Z., Koltun, V.: Playing for benchmarks. In: Intl. Conf. on Computer Vision (ICCV). (2017)
36. Chang, A.X., Funkhouser, T., Guibas, L., Hanrahan, P., Huang, Q., Li, Z., Savarese, S., Savva, M., Song, S., Su, H., Xiao, J., Yi, L., Yu, F.: ShapeNet: An Information-Rich 3D Model Repository. Technical Report arXiv:1512.03012 [cs.GR], Stanford University — Princeton University — Toyota Technological Institute at Chicago (2015)
37. Su, H., Qi, C.R., Li, Y., Guibas, L.J.: Render for CNN: viewpoint estimation in images using cnns trained with rendered 3d model views. In: The IEEE International Conference on Computer Vision (ICCV). (December 2015)
38. Dosovitskiy, A., Fischer, P., Ilg, E., P, H., xE, usser, Hazirbas, C., Golkov, V., Smagt, P.v.d., Cremers, D., Brox, T.: FlowNet: Learning optical flow with convolutional networks. In: Intl. Conf. on Computer Vision (ICCV). (2015) 2758–2766
39. Loper, M., Mahmood, N., Romero, J., Pons-Moll, G., Black, M.J.: SMPL: A skinned multi-person linear model. SIGGRAPH Asia **34**(6) (October 2015) 248:1–248:16
40. Hartley, R.I., Zisserman, A.: Multiple View Geometry in Computer Vision. Second edn. Cambridge University Press, ISBN: 0521540518 (2004)
41. Nistér, D.: Preemptive ransac for live structure and motion estimation. In: Proceedings of the Ninth IEEE International Conference on Computer Vision - Volume 2. ICCV '03, Washington, DC, USA, IEEE Computer Society (2003) 199–
42. Sevilla-Lara, L., Sun, D., Jampani, V., Black, M.J.: Optical flow with semantic segmentation and localized layers. In: IEEE Conf. on Computer Vision and Pattern Recognition (CVPR). (June 2016)
43. Dai, A., Nießner, M., Zollöfer, M., Izadi, S., Theobalt, C.: BundleFusion: real-time globally consistent 3D reconstruction using on-the-fly surface re-integration. ACM Transactions on Graphics 2017 (TOG) (2017)
44. Handa, A., Whelan, T., McDonald, J., Davison, A.: A benchmark for RGB-D visual odometry, 3D reconstruction and SLAM. In: IEEE Intl. Conf. on Robotics and Automation (ICRA), Hong Kong, China (May 2014)

45. Xiao, J., Owens, A., Torralba, A.: SUN3D: a database of big spaces reconstructed using SfM and object labels. In: Intl. Conf. on Computer Vision (ICCV), Los Alamitos, CA, USA, IEEE Computer Society (2013) 1625–1632
46. Ionescu, C., Papava, D., Olaru, V., Sminchisescu, C.: Human3.6M: large scale datasets and predictive methods for 3d human sensing in natural environments. *IEEE Trans. Pattern Anal. Machine Intell.* **36**(7) (jul 2014) 1325–1339
47. Pons-Moll, G., Romero, J., Mahmood, N., Black, M.J.: Dyna: A model of dynamic human shape in motion. *SIGGRAPH* **34**(4) (August 2015) 120:1–120:14
48. Dellaert, F.: Factor graphs and GTSAM: a hands-on introduction. Technical Report GT-RIM-CP&R-2012-002, GT RIM (Sept 2012)
49. He, K., Zhang, X., Ren, S., Sun, J.: Delving deep into rectifiers: Surpassing human-level performance on imagenet classification. In: Proceedings of the 2015 IEEE International Conference on Computer Vision (ICCV). Intl. Conf. on Computer Vision (ICCV), Washington, DC, USA, IEEE Computer Society (2015) 1026–1034
50. Sturm, J., Engelhard, N., Endres, F., Burgard, W., Cremers, D.: A benchmark for the evaluation of rgb-d slam systems. In: IEEE/RSJ Intl. Conf. on Intelligent Robots and Systems (IROS). (Oct. 2012)
51. Mur-Artal, R., Tards, J.D.: ORB-SLAM2: an open-source SLAM system for monocular, stereo and RGB-D cameras. *CoRR* **abs/1610.06475** (2016)
52. Chen, L.C., Papandreou, G., Kokkinos, I., Murphy, K., Yuille, A.L.: Deeplab: Semantic image segmentation with deep convolutional nets, atrous convolution, and fully connected crfs. *arXiv:1606.00915* (2016)
53. Green, R.: Spherical Harmonic Lighting: The Gritty Details. Archives of the Game Developers Conference (March 2003)

Appendices

A Visualization for Qualitative Evaluation

Color coding for flow vectors We visualize the flow vectors in 2D following the color encoding in [31], for optical flow $\delta\mathbf{u}_{0\rightarrow 1}^{of}$, egomotion flow $\delta\mathbf{u}_{0\rightarrow 1}^{cm}$ and projected scene flow $\delta\mathbf{u}_{0\rightarrow 1}^{sf}$. The central white color means there is no motion. Hue represents the flow vector direction, and color intensity represents the magnitude. All the flow vectors are normalized to the range [0,1] during visualization, shown in Figure 8. Thus, an accurate estimation of flow should have minimal difference w.r.t. ground truth flow visualization both in hue and intensity.



Fig. 8: **Flow color encoding** in all qualitative visualizations. The central white color means there is no motion. Hue represents the flow vector direction and color intensity represents the magnitude. All the flow vectors are normalized to the range of 0-1 during visualization.

We visualize the 3D dense scene flow following the same color encoding in 2D, simply by using the corresponding projected scene flow $\delta\mathbf{u}_{0\rightarrow 1}^{sf}$ per-pixel. Such color encoding in projected image space can alleviate the noisy estimation for depth close to infinity, which usually has huge uncertainty in scale and thus affects the magnitude normalization.

B Training Optical Flow with REFRESH Dataset

We evaluate our optical flow model [15] trained on REFRESH dataset and compare it against models trained on FlyingChairs [38] and FlyingThings3D [33]. This evaluation serves as a sanity check of our dataset, and more importantly, an indication of its usefulness for scene flow.

Admittedly, the comparison with FlyingChairs [38] is not apple-to-apple. First, the FlyingChairs dataset is for 2D optical flow because it does not provide information such as depth, foreground masks, and camera ego-motion. More critically, the dataset has been tuned to match the statistics of the synthetic SINTTEL dataset. However, it is important to check how valid our new dataset is for 2D optical flow, which is a sub-task of scene flow. As discussed earlier, the Fly-

Table 3: **Optical flow validation comparison** (EPE) on SINTEL[31] set (all images) using different datasets as training from scratch, validated at different number of training iterations. The same PWC-net [15] architecture is use in all training.

SINTEL EPE (clean/final)	6K	30K	60K	90K	120K
FlyingChairs[38]	6.87/7.58	4.27/5.22	3.75/4.66	3.42/4.50	3.36/4.43
FlyingThings3D [33]	8.98/9.89	6.14/7.11	5.57/6.63	5.26/6.28	5.13/6.11
REFRESH (Ours)	5.82/6.54	4.27/5.23	3.85/4.78	3.45/4.48	3.42/4.46

ingThings3D dataset is the only training dataset that satisfies the requirements for training scene flow models³.

As shown in Table 3, REFRESH dataset converges significantly faster and achieves better results on SINTEL than the FlyingThings3D dataset. The model trained on the REFRESH dataset also has similar performance as the one trained on the FlyingChairs dataset.

C REFRESH Datasets

C.1 Dataset rendering details

The whole dataset creation is done using Blender 2.78⁴, fully automated with python scripts without any GUI interaction, which scales well to the creation of the entire dataset. We separately render the background 3D meshes and foreground nonrigid humans, which allows us to speed up the rendering process. Since we use the raw color image as the background image and only use the geometry ground truth from multi-pass rendering (depth, flow, and segmentation), lighting does not affect background rendering with or without the foreground. Such separation can significantly boost the dataset creation speed. With a 28-core CPU server, we can finish the entire rendering process using BundleFusion [43] 3D scenes in two days.

Background Static Mesh Rendering Since we do not use the rendered color images in any process, we use a simplified setting for background rendering without ray-tracing, tile size as 512×512 . The rendering time depends on the size of 3D mesh size. In average, we render one frame in ($< 1s$) in CPU, and we can finish the frame-by-frame rendering of 8 scenes of BundleFusion in 10 hours.

Foreground Nonrigid Human Rendering We create the human bodies following SURREAL [16] with synthetic textures (772 clothes textures and 158 CAESAR textures). The illuminated textures are used as the appearance of humans in our composited dynamic scenes. We use spherical harmonics with nine coefficients [53], with ambient illumination coefficient randomly sampled from [0.5, 1.5] and other coefficients randomly sampled from [-0.7, 0.7]. We implement this part by refactoring over [16], by extending SURREAL to arbitrary humans bodies with random textures and actions.

³ The Sintel dataset is held for validation and contains much fewer sequences to train scene flow models from scratch.

⁴ Blender: <https://www.blender.org/>

We split the camera trajectory into multiple clips. Each clip is a continuous 100-frame sequence, with randomly loaded human models and actions. There are two major motivations to rendering the outputs in clips rather than an entire trajectory: 1. We can load different random human bodies and motions for different clips in the same trajectory, which increase the motion diversity both in action and appearance; 2. There are numerous human models generated along the entire trajectory, which composes complex meshes in 3D and slow for rendering. Rendering individual clip with several human models is much faster in execution. We can render multiple pass image ground truth with an average of 3 seconds per frame.

Create Ground Truth We use Blender Cycles rendering passes to extract the per-pixel ground truth. We use the *Vector* node to retrieve the 2D vectors giving the frame by frame motions towards to the next and previous frame positions in pixel space, which are denoted as the forward/backward optical flow. Note that we currently do not retrieve the 3D motion vector representation of scene flow from Blender as one pass, which can be an extension to the current dataset in the future work.

We use the rendered depth from 3D scenes instead of the raw 3D scene depth for all the training. Compared to the raw depth, the rendered depth is less noisy and contains less missing measurements and has a per-pixel correspondence to the other ground truth, e.g., optical flow. However, the rendered depth does not guarantee a valid per-pixel value due to the incomplete 3D reconstruction from raw measurements. We marked the projected pixels from incomplete regions (holes in 3D reconstruction) as *invalid* region, and exclude them from the training on-the-fly.

C.2 Dataset statistics

We rendered dataset using the optimized camera trajectory during 3D reconstruction as the camera extrinsic setting. Since the camera movement during 3D acquisition is small and stable between frames, we also use the sampled keyframes from the camera trajectory during rendering. We name the sub-sample trajectory based on their frame interval n as *keyframe n*: *keyframe1* represents that we use every frame along the trajectory during dataset creation and *keyframe10* represents we use every ten frames. We list the number of static scene frames with varying keyframes in Table 4.

Figure 9 shows the histogram distributions of our outputs in optical flow, depth, and rigidity from the rendered REFRESH dataset. We show the histogram distribution independently for the data rendered from different keyframes (1,2,5). Compare different keyframe splits, the distribution in depth and non-rigid area ratio in the images are similar and when using larger keyframes, the output optical flow tends to have a larger displacement. When using rendered outputs from larger keyframes, we can simulate the observations from a camera with larger motions.

During training, we empirically find the network generalize the best when using keyframe [1,2,5] from the optimized trajectory from BundleFusion. We use

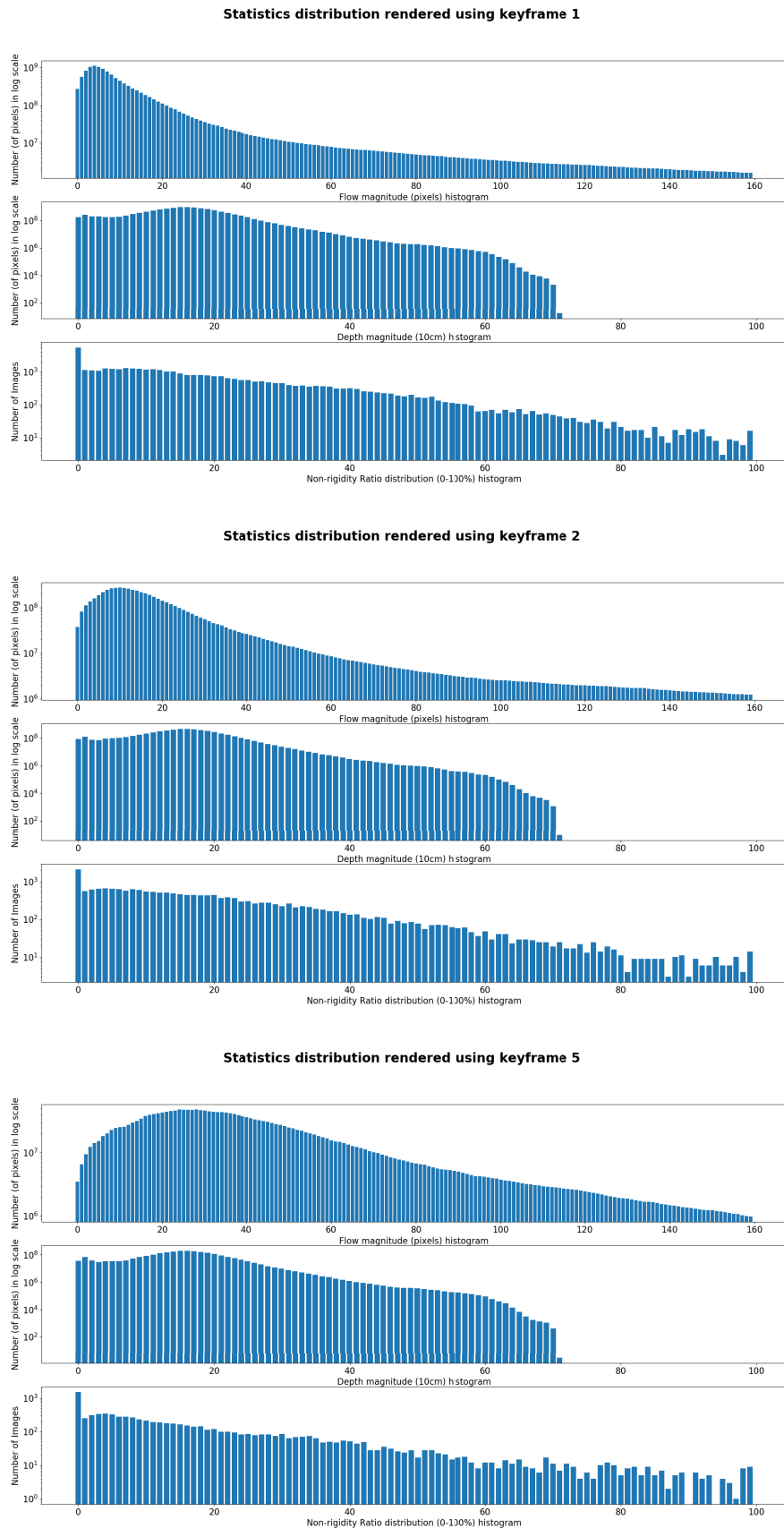


Fig. 9: Histogram distributions of optical flow, depth, and rigidity from our rendered REFRESH dataset in the training set. We calculate the distribution from three splits using keyframes 1, 2, 5 independently. In each of the split, we show the flow magnitude distribution (top) in pixels, depth distribution (medium) in centimeters, and nonrigid ratio (belows) in the number of different images.

the first seven scenes in BundleFusion as our training set ('apt0', 'apt1', 'apt2', 'copyroom', 'office0', 'office1', 'office2') as our training set with a total of 69218 pairs of frames, and use 'office3' as the validation set with 6390 pairs of frames.

C.3 Visualization

We visualize some examples of our datasets in Figure 10 across different scenes. The invalid regions are visualized as black in the depth image and white in the ground truth optical flow.

D Evaluation on SINTEL Dataset

Quantitative Evaluation on Entire SINTEL Dataset

We evaluate our method using RTN and refine step on the all frames in entire SINTEL dataset compared to the two baseline methods in the paper as a supplement to the comparison in our test set split. First one is *refinement only*, which we denote as solving the refinement stage without any information acquired from RTN. Secondly, we compare our method to semantic rigidity estimation [14], which assumes that the non-rigid motion can be predicted from its semantic labeling. The semantic network is trained using the DeepLab [52] architecture with weights initialized from the pre-trained MS-COCO model on the same data we used for our model. In the pose refinement stage, we substitute our rigidity from RTN with the semantic rigidity. Both baselines use the same optical flow network with the same weights, and all methods use the same depth from SINTEL ground truth. We use the EPE in egomotion flow and projected scene flow as a metric. To exclude the effects of some catastrophic failures in some particular frames, we exclude those frames that have over 100 EPE values and separately count them as failure cases. None of the models are finetuned on SINTEL dataset. Table 5 shows the quantitative evaluation. It is worth to note that predicting rigidity based on semantics cannot generalize well across different domains, which can lead to bad rigidity localization that significantly harm the correspondence association. This evaluation also shows our method outperforms the two baseline methods.

Table 4: The number of rendered images generated in our REFRESH dataset using BundleFusion [43] as 3D scenes.

	apt0	apt1	apt2	copyroom	office0	office1	office2	office3	Total
keyframe 1	8560	8495	3873	4478	6083	5727	3494	3757	44467
keyframe 2	4280	4248	1937	2239	3043	2863	1748	1882	22240
keyframe 5	1712	1700	776	895	1220	1146	700	752	8901
keyframe 10	856	849	338	447	609	572	349	376	4446
keyframe 20	427	424	195	223	304	286	174	189	2222
keyframe 50	171	169	78	89	123	114	69	75	888
Total	16006	15885	7247	8371	11382	10708	6534	5149	83164

Background scenes (color images), used in final composition



Rendered scenes (color images, not used in final composition)



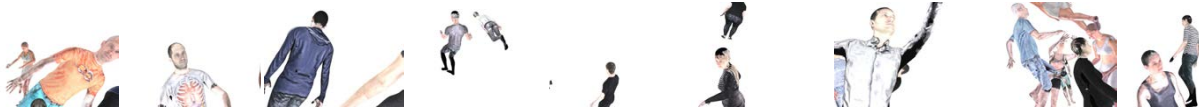
Background scenes (raw depth images, not used in final composition)



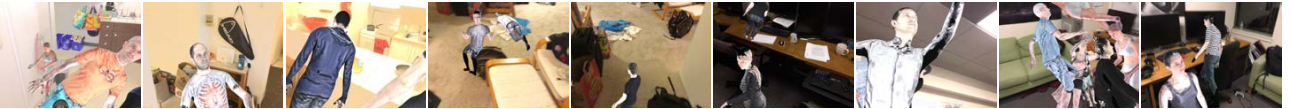
Rendered scenes (depth images, used in final composition)



Nonrigid scenes (color images)



Composited dynamic Scenes (color images)



Composited dynamic Scenes (depth images)



Ground truth in optical flow



Ground truth in rigidity mask (non-rigid region in white)



Fig. 10: Qualitative visualization of Frames in REFRESH Datasets.

Table 5: Quantitative Evaluation on SINTEL dataset using all frames. All models in this evaluation are *not finetuned* and trained on REFRESH dataset. We report the EPE in egomotion flow (EF) and projected scene flow (PSF). The number in *failures* indicate the number of frames that has an EPE over 100, which is excluded in the EPE calculation. For all the baseline methods, we use the same optical flow network trained as our method. The lowest residual under the same setting (e.g. clean set) is highlighted as **bold**.

	Final Pass All			Clean Pass All		
	EF	PSF	failures	EF	PSF	failures
Refine (from flow only)	2.71	6.81	19	2.61	6.67	9
Semantic rigidity [14] + refine	6.19	9.35	25	4.57	7.68	12
RTN + Refine	1.78	5.81	17	1.75	5.72	6